

Contents lists available at [ScienceDirect](http://www.sciencedirect.com)

Journal of the Mechanics and Physics of Solids

journal homepage: www.elsevier.com/locate/jmps

A hierarchical computational model for stretchable interconnects with fractal-inspired designs



Yihui Zhang^{a,b,1}, Haoran Fu^{a,c,1}, Sheng Xu^d, Jonathan A. Fan^d,
Keh-Chih Hwang^b, Jianqun Jiang^c, John A. Rogers^d, Yonggang Huang^{a,*}

^a Departments of Civil and Environmental Engineering and Mechanical Engineering, Center for Engineering and Health, Skin Disease Research Center, Northwestern University, Evanston, IL 60208, USA

^b Center for Mechanics and Materials, Tsinghua University, Beijing 100084, China

^c Department of Civil Engineering and Architecture, Zhejiang University, Hangzhou 310058, China

^d Department of Materials Science and Engineering, Frederick Seitz Materials Research Laboratory, University of Illinois at Urbana-Champaign, Urbana, IL 61801, USA

ARTICLE INFO

Article history:

Received 30 December 2013

Received in revised form

4 May 2014

Accepted 28 July 2014

Available online 12 August 2014

Keywords:

Hierarchical computational model

Fractal interconnects

Ordered unraveling

Postbuckling

ABSTRACT

Stretchable electronics that require functional components with high areal coverages, antennas with small sizes and/or electrodes with invisibility under magnetic resonance imaging can benefit from the use of electrical wiring constructs that adopt fractal inspired layouts. Due to the complex and diverse microstructures inherent in high order interconnects/electrodes/antennas with such designs, traditional non-linear postbuckling analyses based on conventional finite element analyses (FEA) can be cumbersome and time-consuming. Here, we introduce a hierarchical computational model (HCM) based on the mechanism of ordered unraveling for postbuckling analysis of fractal inspired interconnects, in designs previously referred to as ‘self-similar’, under stretching. The model reduces the computational efforts of traditional approaches by many orders of magnitude, but with accurate predictions, as validated by experiments and FEA. As the fractal order increases from 1 to 4, the elastic stretchability can be enhanced by ~200 times, clearly illustrating the advantage of simple concepts in fractal design. These results, and the model in general, can be exploited in the development of optimal designs in wide ranging classes of stretchable electronics systems.

© 2014 Elsevier Ltd. All rights reserved.

1. Introduction

Recent advances in mechanics and materials for stretchable/flexible electronics (Lacour et al., 2005; Khang et al., 2006; Lacour et al., 2006; Jiang et al., 2007, 2008; Sekitani et al., 2009; Rogers et al., 2010; Huang et al., 2012; Yang and Lu, 2013; Duan et al., 2014) and optoelectronics (Kim et al., 2010; Lee et al., 2011a; Lipomi et al., 2011; Nelson et al., 2011) demonstrate that systems with high-performance semiconductor functionality can be realized in forms that allow extreme mechanical deformations, e.g., stretching like a rubber band, twisting like a rope, and bending like a sheet of paper. This class of technology creates many application opportunities that cannot be addressed with established technologies, ranging from “epidermal” health/wellness monitors (Kim et al., 2011b; Kaltenbrunner et al., 2013; Schwartz et al., 2013), to soft surgical

* Corresponding author at: Department of Civil and Environmental Engineering, Center for Engineering and Health, Skin Disease Research Center, Northwestern University, Evanston, IL 60208, USA.

E-mail address: y-huang@northwestern.edu (Y. Huang).

¹ These authors contributed equally to this work.

instruments (Cotton et al., 2009; Yu et al., 2009; Viventi et al., 2010; Graudejus et al., 2012; Kim et al., 2012b), to eyeball-like digital cameras (Ko et al., 2008; Song et al., 2013), to sensitive robotic skins (Someya et al., 2004; Wagner et al., 2004; Mannsfeld et al., 2010; Lu et al., 2012). Many of these stretchable systems exploit a strategy, sometimes known as the island-bridge design (Kim et al., 2008, 2009, 2011b; Ko et al., 2008; Lee et al., 2011b), in which the active devices reside on non-deformable platforms (i.e. islands) with deformable interconnects (i.e. bridges) in between. These bridges provide stretchability, while the islands undergo negligible deformation (usually $< 1\%$ strain) to ensure mechanical integrity of the active devices (Kim et al., 2008; Song et al., 2009). The stretchability of a system with a certain filling ratio of islands can be written by

$$\text{stretchability of the system} = (1 - \sqrt{\text{filling ratio}}) * (\text{stretchability of the interconnect}). \quad (1)$$

where the filling ratio denotes the ratio of area covered by the islands to the entire area of an island-bridge structure. Various types of interconnect technologies have been developed, typically involving planar serpentine (Jones et al., 2004;

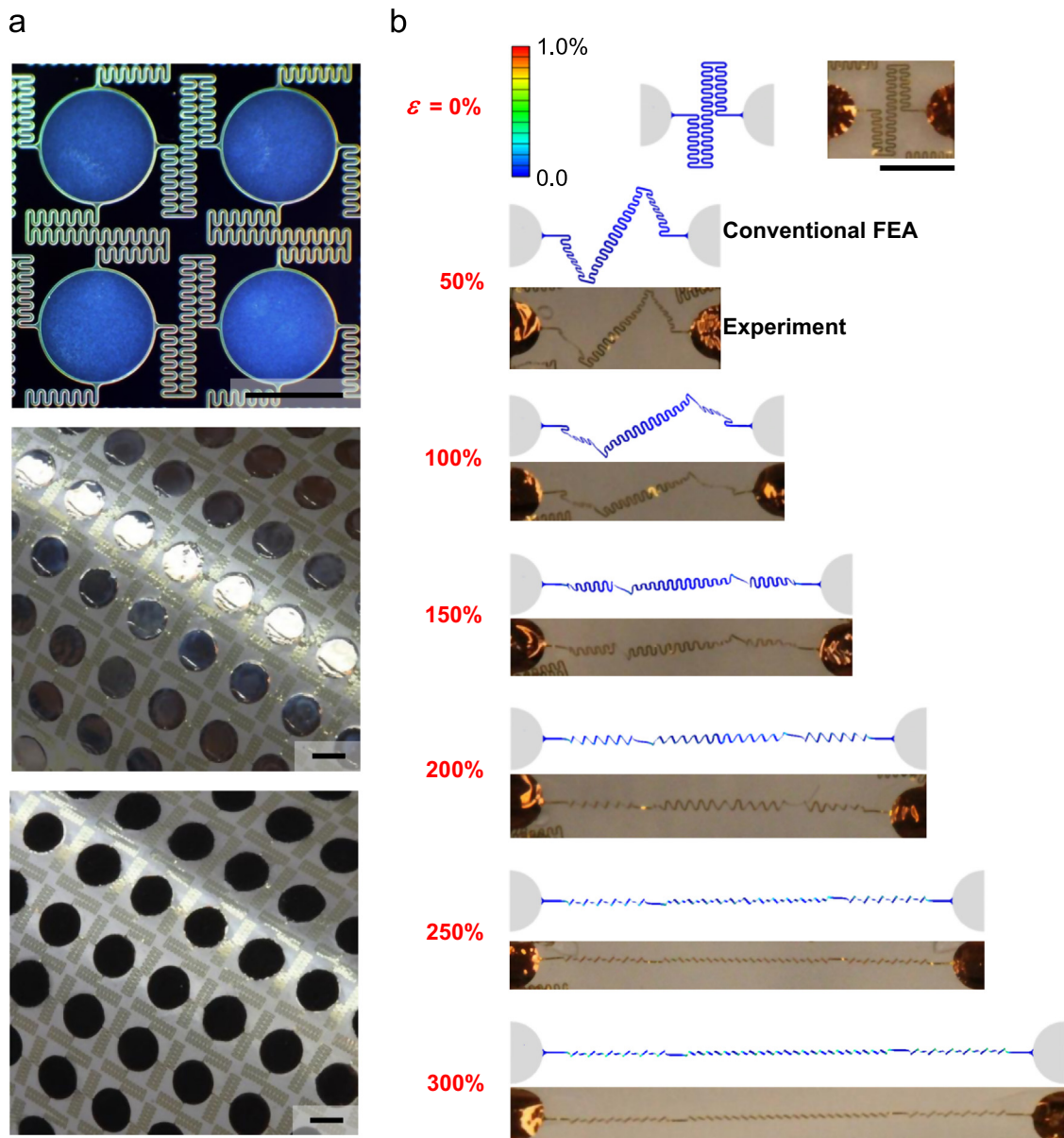


Fig. 1. (a) Optical images of electrode pads and fractal inspired interconnects on a silicon wafer (top panel; top down view; ~ 4 unit cells), after transfer printing on a sheet of silicone (middle panel; oblique view, in a bent geometry), and with molded slurries of LiCoO₂ (bottom panel; oblique view, in a bent geometry), for a stretchable Li-ion battery; (b) optical images and corresponding conventional FEA results of symmetric deformation modes, for various levels of applied tensile strain ϵ . The scale bars in (a) and (b) are 2 mm. (a and b) Are reprinted with permission from Xu et al. (2013), Copyright 2013, Nature Publishing Group.

Lacour et al., 2005; Li et al., 2005; Gonzalez et al., 2008; Kim et al., 2008, 2011b, 2012c; Hsu et al., 2009; Zhang et al., 2013b) or non-coplanar serpentine or straight bridges (Kim et al., 2008; Ko et al., 2008; Lee et al., 2011b). In many published examples, such interconnects offer total stretchability $< 50\%$ (defined by onset of cracks) and elastic stretchability $< 25\%$ (defined by onset of plastic deformation), in systems that do not significantly sacrifice the filling ratio. Many applications, particularly those in optoelectronics (Ko et al., 2008; Kim et al., 2010) and energy storage systems (Lipomi et al., 2011; Xu et al., 2013), also require high filling ratios. Here, advanced interconnects are needed.

Recently, Xu et al. (2013) reported a design based on a type of space-filling curve that incorporates serpentine patterns in simple fractal-inspired layouts (shown in Fig. 1a), to address the aforementioned challenges. The hierarchical structures with fractal inspired layouts have been shown to exist in many biological systems (Gao et al., 2005; Yao and Gao, 2006, 2007; Zhang et al., 2011, 2012; Li et al., 2012, 2013), which could enhance or even control the surface adhesions, stiffness and material strengths. This technology, referred to initially as a ‘self-similar’ design (Xu et al., 2013), enables stretchable lithium-ion batteries with total stretchability and elastic stretchability of $\sim 300\%$ and $\sim 160\%$, respectively, and a filling ratio of $\sim 33\%$. The underlying mechanisms responsible for this favorable mechanics were studied by both experiments and finite element analyses (FEA), as shown in Fig. 1b. The results reveal a mechanism of ordered unraveling. Specifically, with the stretching proceeds from 0% to $\sim 150\%$, the 2nd order structure (i.e., the large spring) first unravels via out-of-plane bending and twisting through buckling, during which there is essentially no deformation in the 1st order structure (i.e., the small spring) (see top 4 images, Fig. 1b). The unraveling of the 1st order structure only starts as the 2nd order structure is fully extended, corresponding to an applied strain of $\sim 150\%$. Additional, large stretchability ($\sim 300\%$) is then achieved when the 1st order structure is stretched to nearly its maximum extent (see bottom 3 images, Fig. 1b). Only the active materials are bonded to the soft substrate in this battery design such that the interconnects can deform freely. For some biomedical applications (Kim et al., 2011b, 2012c), the serpentine interconnects are either bonded to or encapsulated in the soft substrate, and the resulting deformation mechanism may be quite different from the free standing interconnects (Zhang et al., 2014), but such aspects are beyond the scope of the present study.

The filling ratio of active devices in the island-bridge design shown in Fig. 1a is 33%. The elastic stretchability ($\sim 150\%$) is reduced to 22% and 4.3% for filling ratios of 90% and 98%, respectively. These levels of elastic stretchability fall short of some biomedical applications, such as those in skin-mounted electronics (Kim et al., 2011b; Ying et al., 2012; Webb et al., 2013)

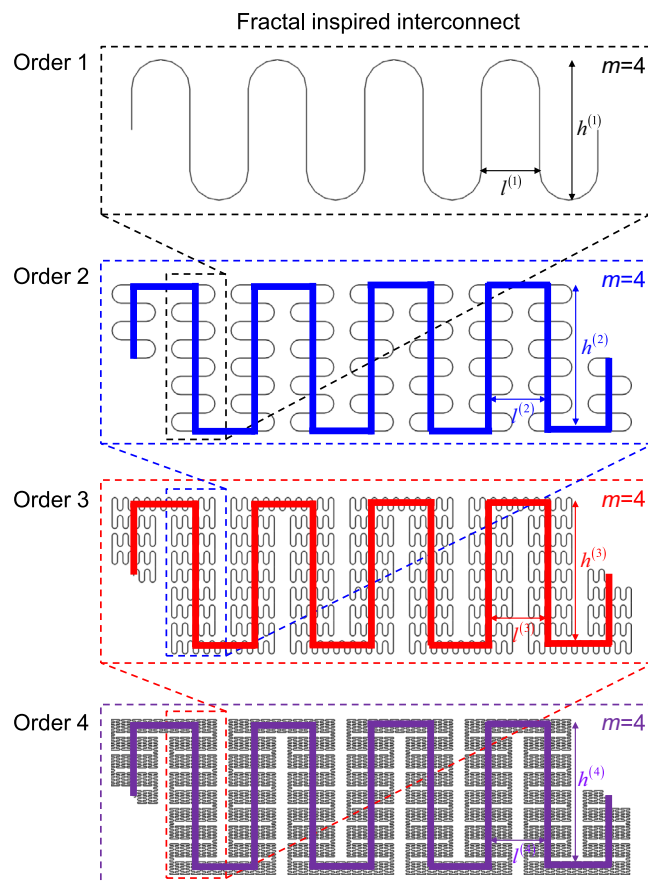


Fig. 2. Schematic illustration of the geometric construction of a fractal inspired interconnect. (For interpretation of the references to color in this figure, the reader is referred to the web version of this article.)

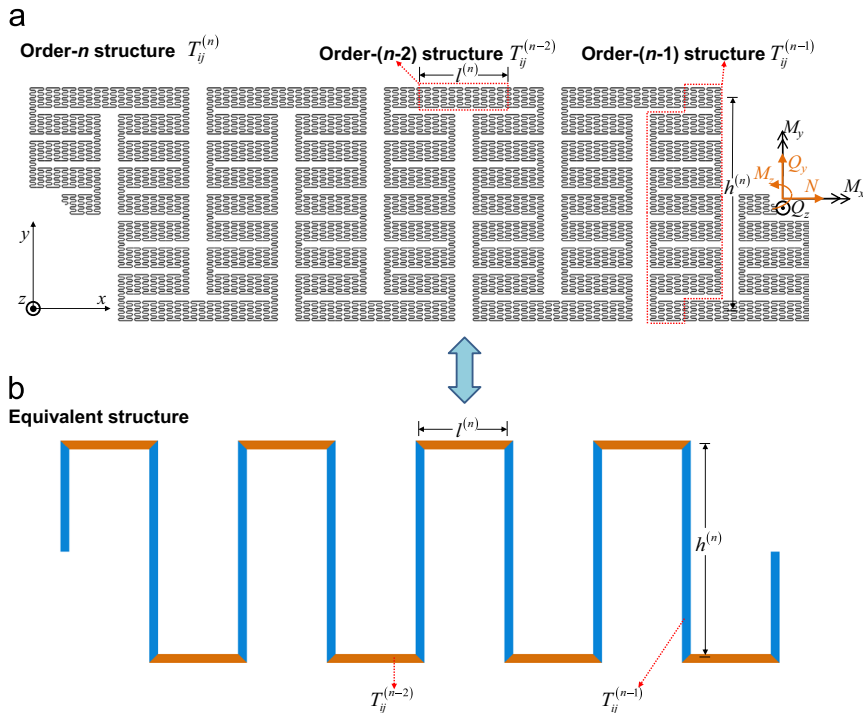


Fig. 3. Schematic illustration of the equivalent structure for a fractal inspired interconnect: (a) an order- n fractal interconnect composed of vertically aligned order- $(n-1)$ interconnects, and horizontally aligned order- $(n-2)$ interconnects and (b) equivalent structure consisting of only straight beams. (For interpretation of the references to color in this figure, the reader is referred to the web version of this article.)

and inflatable catheter technology (Kim et al., 2011a, 2012a), in which the strains (e.g., skin, heart, or elbow) may well exceed 20%. The most viable solution is to increase the fractal order, from 2 in Figs. 1a to 3 and 4 in Fig. 2 or even higher. For the fractal order of 4, however, the conventional FEA approach becomes prohibitively time-consuming because of the large number of elements (> 1 million) and the highly non-linear postbuckling analysis. Such a computational approach is impractical for rapid device design and optimization.

The aim of the present study is to develop an effective and robust hierarchical computational model (HCM), based on the mechanism of ordered unraveling illustrated in Fig. 1, for postbuckling analysis of serpentine interconnects with fractal inspired layouts (referred to as “fractal interconnects” in the following). For an order- n fractal interconnect under stretching, the lower order structures ($\leq n-1$) initially do not unravel, and are only bent and twisted. As a result, these lower order structures can be modeled as straight beams with effective tension, bending and torsion flexibilities, as illustrated in Fig. 3. Once the highest (n)th order structure is fully stretched, unraveling of $(n-1)$ th order structure starts, but the $(n-2)$ th and lower order structures still do not unravel and can be modeled as beams. This process continues until the 1st order structure unravels and the total stretchability is finally reached. Such an approach substantially saves computational effort because, at each order, only bending and twisting of straight beams is involved. This simplification enables simulations of high order (up to 4 as we demonstrated herein) fractal interconnects, which would be quite difficult by using the conventional FEA. This set of calculations not only illustrates the significant effect of fractal order on stretchability, but also provides reference for design using high-order fractal interconnects. The paper is outlined as follows. Section 2 determines the equivalent flexibilities for any order ($n \geq 2$) of fractal interconnect. Section 3 describes the HCM for ordered unraveling of the postbuckling process. Section 4 applies the HCM to study the effect of fractal order on the elastic stretchability. Generalized fractal interconnects are studied in Section 5, and the results are validated by experiments and conventional FEA.

2. Equivalent flexibilities of fractal interconnects

2.1. Geometry

The 1st order interconnect consists of straight wires and half circles that are connected in series, as shown in the black box of Fig. 2, which has 4 unit cells in this example. The 2nd order interconnect, shown in the blue box of Fig. 2, is created by reducing the scale of the 1st order interconnects, followed by 90° rotation, and then connecting them in a fashion that reproduces the layout of the original geometry. The wide blue line in Fig. 2 represents the 2nd order geometry that is similar to the 1st order geometry (except for the rounded part). By implementing the same procedure, we can generate the 3rd and 4th order interconnects, as illustrated in the red and purple boxes of Fig. 2, where the red and purple lines denote the 3rd

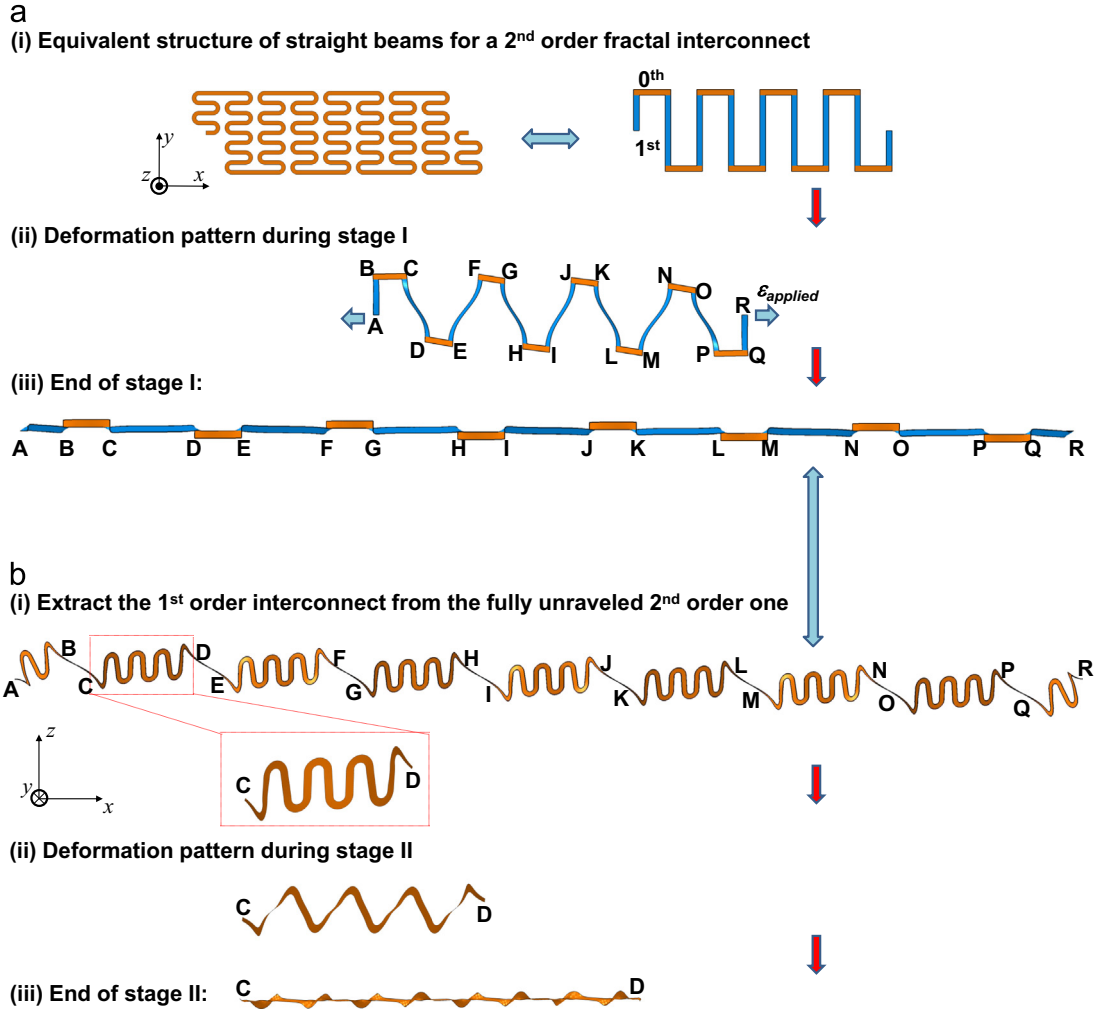


Fig. 4. Illustration of the hierarchal computational model (HCM) for a 2nd order fractal interconnect: (a) Stage I – unraveling the 2nd order structure, in which the entire interconnect is modeled by an equivalent structure of straight beams; and (b) Stage II – unraveling each 1st order structure, studied using the original geometry of the structure. (For interpretation of the references to color in this figure, the reader is referred to the web version of this article.)

and 4th order geometries, respectively. It is clear that the 2nd to 4th (and higher) order geometries all exhibit the same rectangular shape, and have the same number of unit cells, which indicates that, strictly speaking, the fractal only starts at the 2nd order.

Let η denote the height/spacing aspect ratio at each order such that the height $h^{(i)}$ is related to the spacing $l^{(i)}$ of the i th ($i = 1 \dots n$) order (Fig. 2) by $h^{(i)} = \eta l^{(i)}$. The height $h^{(i)}$ is also related to the spacing $l^{(i-1)}$ of the neighboring order by the number of unit cells m (Fig. 2) as $h^{(i)} = 2ml^{(i-1)}$ ($i = 2 \dots n$). The spacing and height at any order i are then scaled with the spacing of the highest order $l^{(n)}$ by

$$l^{(i)} = \left(\frac{\eta}{2m}\right)^{n-i} l^{(n)}, \quad h^{(i)} = \eta \left(\frac{\eta}{2m}\right)^{n-i} l^{(n)} \quad (i = 1 \dots n) \tag{2}$$

The result shows that a fractal interconnect is characterized by one base length ($l^{(n)}$) and three non-dimensional parameters, namely the fractal order (n), the height/spacing ratio (η) and number (m) of unit cell.

2.2. Equivalent flexibilities

A fractal interconnect can be modeled as a beam if its width (w) and thickness (t) are much smaller than the length. Fig. 3a shows an n th order fractal interconnect clamped at the left end, and subject to forces and bending moments at the right end. The axial force N , in-plane shear force Q_y and bending moment M_z at the right end induce the in-plane deformation represented by the displacements u_x and u_y and rotation θ_z at the end, while the out-of-plane shear force Q_z and bending moment M_y , and torque M_x at the right end generate the out-of-plane displacement u_z and rotations θ_x and θ_y .

at the end. The normalized displacements, rotations, forces, bending moments and torques are related by

$$\begin{pmatrix} u_x/l^{(n)} \\ u_y/l^{(n)} \\ \theta_z \end{pmatrix} = \mathbf{T}_{in-plane}^{(n)} \begin{pmatrix} N[l^{(n)}]^2/(EI)_{in-plane} \\ Q_y[l^{(n)}]^2/(EI)_{in-plane} \\ M_z l^{(n)}/(EI)_{in-plane} \end{pmatrix}, \quad (3a)$$

$$\begin{pmatrix} u_z/l^{(n)} \\ \theta_y \\ \theta_x \end{pmatrix} = \mathbf{T}_{out-of-plane}^{(n)} \begin{pmatrix} Q_z[l^{(n)}]^2/(EI)_{out-of-plane} \\ M_y l^{(n)}/(EI)_{out-of-plane} \\ M_x l^{(n)}/(EI)_{out-of-plane} \end{pmatrix}, \quad (3b)$$

where $(EI)_{in-plane} = Ew^3t/12$ and $(EI)_{out-of-plane} = Ewt^3/12$ are the in-plane and out-of-plane bending stiffness, respectively, and $\mathbf{T}_{in-plane}^{(n)}$ and $\mathbf{T}_{out-of-plane}^{(n)}$ are the normalized elastic flexibility matrices that can be obtained analytically (see [Appendix A](#)). For example, the in-plane flexibility matrix for the 1st order fractal interconnect is

$$\mathbf{T}_{in-plane}^{(1)}(m, \eta) = \begin{Bmatrix} \frac{m}{24}(4g^3 + 6\pi g^2 + 24g + 3\pi) & & \text{Sym} \\ \frac{m}{4}(g^2 + \pi g + 2) & \frac{4m^3}{3}(2g + \pi) + \frac{m}{24}(8g + \pi) & \\ 0 & 2m^2(g + \pi) & m(2g + \pi) \end{Bmatrix}, \quad (4a)$$

where Sym denotes the symmetric matrix, and $g = \eta - 1$. The out-of-plane flexibility matrix for the 1st order fractal interconnect is

$$\mathbf{T}_{out-of-plane}^{(1)}(m, \eta) = \begin{Bmatrix} \frac{4m^3}{3}k + \frac{m}{48}[4k(3g^2 + 8) - 4(1 + 3\nu)g^3 - 3(7 + \nu)\pi] & & \text{Sym} \\ & -m^2k & mk \\ & 0 & 0 \quad m[k + (1 - \nu)g] \end{Bmatrix}, \quad (4b)$$

where ν is Poisson's ratio, and $k = [4(1 + \nu)g + (3 + \nu)\pi]/4$. For the 2nd order fractal interconnect, the in-plane flexibility matrix is

$$\mathbf{T}_{in-plane}^{(2)}(m, \eta) = \begin{Bmatrix} \frac{m}{4}\eta^2(4 - p) + \frac{\eta^3}{4m^2}T_{in-plane,22}^{(1)} & & \text{Sym} \\ \frac{m}{8}\eta(p + 2) & \frac{4m^3}{3}p + \frac{m}{6}(p - 2) + \frac{\eta^3}{4m^2}T_{in-plane,11}^{(1)} & \\ 0 & m^2p & mp \end{Bmatrix}, \quad (5a)$$

where $p = 2\eta^2 + (\pi - 2)\eta + 2$, $T_{in-plane,11}^{(1)}$ and $T_{in-plane,22}^{(1)}$ are the 11 and 22 components in Eq. (4a), corresponding to the tensile and in-plane shear flexibilities, respectively. The out-of-plane flexibility matrix for the 2nd order fractal interconnect is

$$\mathbf{T}_{out-of-plane}^{(2)}(m, \eta) = \begin{Bmatrix} T_{out-of-plane,11}^{(2)} & & \text{Sym} \\ -m^2(p - \frac{1-\nu}{4}\pi\eta) & m(p - \frac{1-\nu}{4}\pi\eta) & \\ 0 & 0 & m(\frac{1+\nu}{2}p + \frac{1-\nu}{4}\pi\eta) \end{Bmatrix}, \quad (5b)$$

where $T_{out-of-plane,11}^{(2)}$ is given in [Appendix A](#). For the higher order ($n \geq 3$) fractal interconnects, $\mathbf{T}_{in-plane}^{(n)}$ and $\mathbf{T}_{out-of-plane}^{(n)}$ are obtained in a recursive formula via the flexibility matrices for the $(n-1)$ th and $(n-2)$ th order (see [Appendix A](#)).

The flexibilities obtained from (Eqs. (4) and 5) and the recursive formula in [Appendix A](#) increase with the fractal order. For example, the tensile component $T_{in-plane,11}^{(n)}(m = 4, \eta = 8/\sqrt{11})$ increases from 15.4 for $n = 1$, to 40.1 for $n = 2$, and to 105 for $n = 3$, i.e., by a factor of 2.6 for each increase of fractal order. These values agree reasonably well with the corresponding FEA results, i.e. 15.3 for $n = 1$, 39.7 for $n = 2$, and 114 for $n = 3$. Considering that the length $l^{(n)}$ also increases with n , the corresponding tensile flexibility (without normalization) increases much more rapidly with the fractal order. For $(EI)_{in-plane} = 7.44 \times 10^{-10} \text{ N m}^2$ and $l^{(1)} = 110 \mu\text{m}$ as in the experiments ([Xu et al., 2013](#)), the tensile flexibility increases from 0.0276 m/N for $n = 1$, to 2.62 m/N for $n = 2$, and to 250 m/N for $n = 3$, i.e., increasing by ~ 100 times for each order increase. The fact that the flexibilities increase very rapidly with the fractal order will play a critical role in the development of the HCM in [Section 3](#).

3. The hierarchical computational model for ordered unraveling of fractal interconnects

As shown in [Fig. 3a](#) for 4 unit cells ($m = 4$), an n th order fractal interconnect is composed of $(n-1)$ th order interconnects oriented along vertical (y) direction, and $(n-2)$ th order interconnects oriented along horizontal (x) direction. Before unraveling of any lower order interconnects, the $(n-1)$ th and $(n-2)$ th order interconnects are modeled as the straight beams (in blue and orange colors, respectively, in [Fig. 3b](#)) with the equivalent flexibilities $\mathbf{T}^{(n-1)}$ and $\mathbf{T}^{(n-2)}$ obtained in [Section 2](#). As shown in the following sections, such an approach gives accurate results, but the computation at each order is very simple since it involves only straight beams.

The 2nd order fractal interconnect shown in Fig. 4 is used as an example to illustrate the approach. The postbuckling process can be classified into two stages.

- (i) *Stage I*: Unraveling of the 2nd order fractal interconnect as shown in Fig. 4a. The vertical, 1st order fractal interconnects are represented by straight beams (blue color in Fig. 4a) with the flexibilities given in Eq. (4). (The horizontal segments, denoted by the brown color in Fig. 4a, are already straight beams.) FEA is used for this equivalent structure of straight beams to determine the overall configuration under stretching. Stage I is complete when the equivalent structure of straight beams is fully unraveled, i.e., the distance between the two ends reaches the total length of all straight beams. The applied strain, $\epsilon_{applied}$, defined by the percentage increase of the distance between the two ends, reaches the critical value ($\epsilon_{cr(1)}^{(2)}$) for a 2nd order fractal interconnect at the end of stage I

$$\epsilon_{cr(1)}^{(2)} = \frac{m(2h^{(2)} + 2l^{(2)})}{2ml^{(2)}} - 1 = \eta. \tag{6}$$

The initially vertical 1st order fractal interconnects (blue color) become approximately horizontal (Fig. 4a) at the end of stage I. Their deformations are essentially the same due to the periodicity of unit cells such that the analysis in stage II can focus on unraveling of a single 1st order fractal interconnect, as discussed in the following.

- (ii) *Stage II*: Unraveling of each 1st order fractal interconnect as shown in Fig. 4b. The stretching in stage II is mainly accommodated by the (horizontally aligned) 1st order fractal interconnects (blue color in Fig. 4a) because their tensile

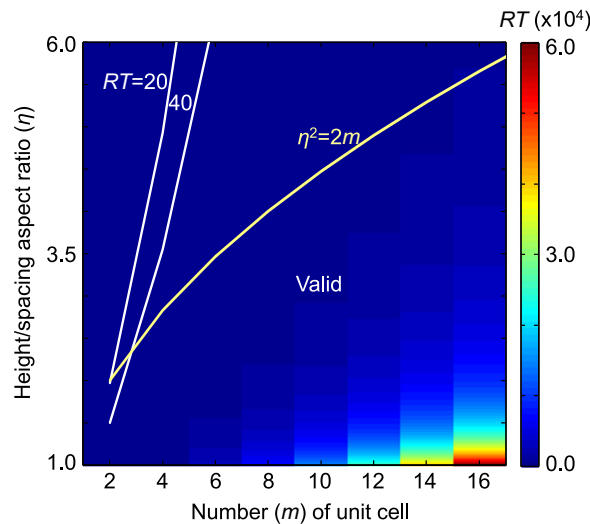


Fig. 5. Distribution of the enhancement ratio (RT) of tensile flexibility in the space of geometric parameters (m and η). The parameter m must be an even number, due to the geometric requirement to construct the fractal serpentine interconnect.

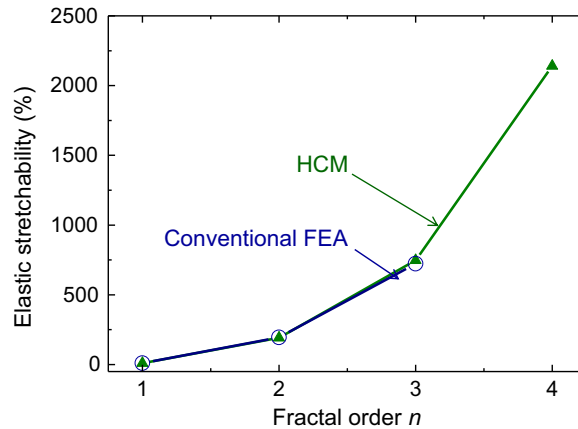


Fig. 6. Elastic stretchability versus the order for fractal interconnects from $n=1$ to 4, with $(m, \eta) = (4, 8/\sqrt{11})$, the thickness/width aspect ratio ($t/w=0.03$), and the width to spacing ratio ($w/l^{(1)}=0.4$), for structures of different fractal orders.

flexibility is much larger than that of straight beams (brown color). Thereby, the deformation of the straight beams is negligible, and only a single 1st order fractal interconnect (e.g., CD in Fig. 4b) is analyzed by FEA (since all 1st order interconnects have essentially the same deformation), which substantially reduces the computational cost. The additional stretching in stage II, $\epsilon_{applied} - \epsilon_{cr(1)}^{(2)}$, corresponds to an additional displacement $2ml^{(2)}[\epsilon_{applied} - \epsilon_{cr(1)}^{(2)}]$ between the two ends of the 2nd order fractal interconnect, which translates to the stretching displacement $l^{(2)}[\epsilon_{applied} - \epsilon_{cr(1)}^{(2)}]$ in the FEA for each 1st order fractal interconnect in stage II. Stage II is complete when each 1st order interconnect is fully unraveled to reach its length $m[2h^{(1)} + (\pi - 2)l^{(1)}]$.

The HCM introduced above is also applicable to higher orders ($n \geq 3$) fractal interconnects. For an order- n fractal interconnect, its (initially vertical) order- $(n - 1)$ and (horizontal) order- $(n - 2)$ interconnects are modeled as straight beams in stage I, followed by unraveling of order- $(n - 1)$ fractal interconnects in stage II. All order- $(n - 2)$ fractal interconnects, which result from both order- n and order- $(n - 1)$ interconnects, start unraveling upon further stretching after stage II. This process

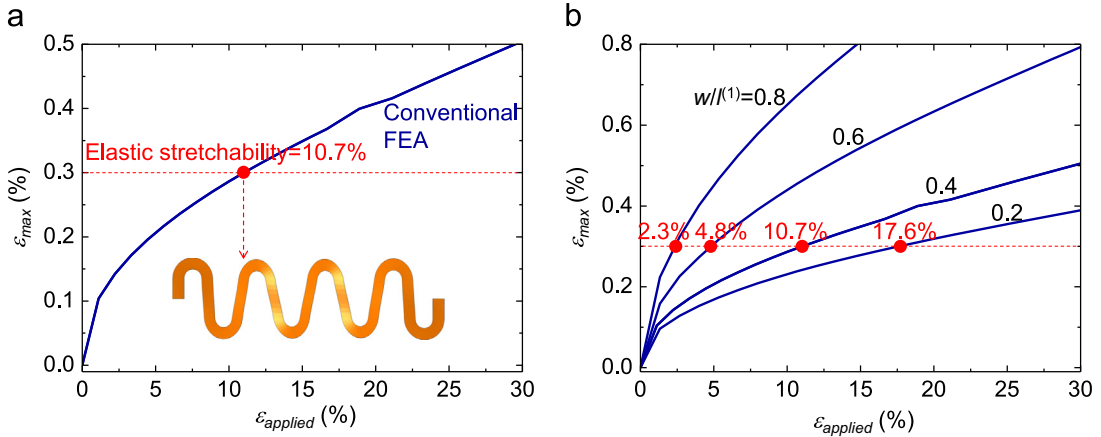


Fig. 7. (a) Maximum principal strain versus the applied strain for a 1st order serpentine interconnect with $(m, \eta) = (4, 8/\sqrt{11})$ and $w/l^{(1)} = 0.4$, where the inset illustrates the deformed pattern of the serpentine interconnect as the elastic stretchability is reached and (b) maximum principal strain versus the applied strain for 1st order serpentine interconnects with $(m, \eta) = (4, 8/\sqrt{11})$, and four different widths ($w/l^{(1)} = 0.2, 0.4, 0.6,$ and 0.8).

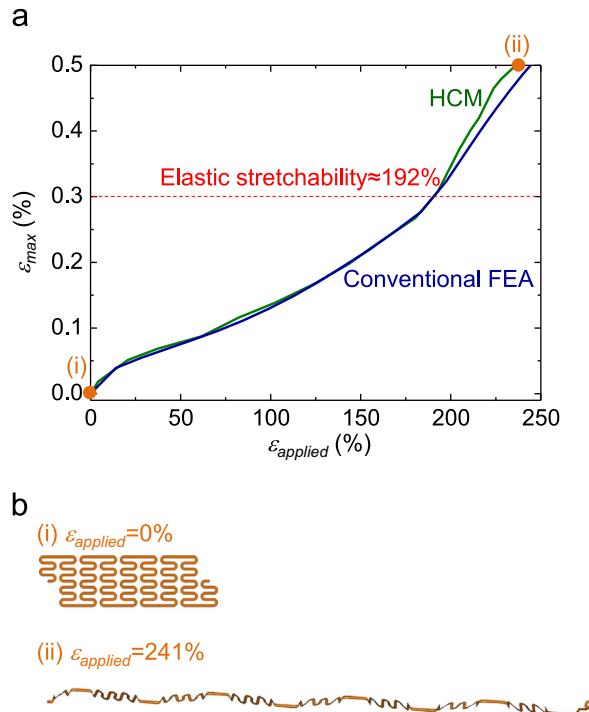


Fig. 8. (a) Maximum principal strain versus the applied strain for a 2nd order fractal interconnect with $(m, \eta) = (4, 8/\sqrt{11})$ and $w/l^{(1)} = 0.4$ and (b) the undeformed and deformed configurations when the 2nd order structure is fully unraveled.

repeats for all lower orders until the 1st-order fractal interconnects unravel. It is clear that the fundamental assumption of this proposed HCM is the mechanism of ordered unraveling, which is mainly resulted from the huge increase of flexibility components at the enhanced level of fractal order. Generally, the ratio of tensile flexibility ($T_{in-plane,11}^{(n)}$, without normalization) at $n=2$ to that at $n=1$ can be obtained from Eqs. (4a) and (5a) as

$$RT = \left(\frac{2m}{\eta}\right)^3 \frac{T_{in-plane,11}^{(2)}}{T_{in-plane,11}^{(1)}} = \frac{2m}{\eta} \frac{24m^2(4-p) + 32m^2\eta(2g+\pi) + \eta(8g+\pi)}{4g^3 + 6\pi g^2 + 24g + 3\pi} \quad (7)$$

This ratio of enhancement is also very close for other increase of fractal order by 1 (e.g., from $n=2$ to 3), due to the self-similar characteristic of the geometry. The fundamental assumption of the HCM should remain valid for a large RT , e.g., > 20 or 40. Fig. 5 shows the distribution of RT in the space of geometric parameters (m and η), in which $\eta^2 < 2m$ should be satisfied to avoid self-overlap of the interconnect. The region of geometric parameters where the HCM is applicable [satisfying $RT > 20$ (or 40) and $\eta^2 < 2m$ simultaneously] is identified. It is clear that the HCM is applicable for most combinations of geometric parameters if $\eta^2 < 2m$.

4. Effect of fractal order on the elastic stretchability and pattern of deformation

The HCM in Section 3 makes it possible to study the postbuckling behavior of high order fractal interconnects with multiple unit cells, as shown in Fig. 2 for the 1st to 4th fractal interconnects with the height/spacing aspect ratio $\eta = 8/\sqrt{11}$ and number of unit cell $m = 4$. The copper interconnect has an elastic modulus $E_{Cu} = 119$ GPa, Poisson’s ratio $\nu_{Cu} = 0.34$, and yield strain 0.3% (William et al., 1999) in an elastic–ideally plastic constitutive model (Hill, 1950). The results are validated by conventional FEA (without any approximations in the HCM) for the fractal order $n \leq 3$ because the analyses of higher order ($n \geq 4$) interconnect would be extremely difficult and time-consuming by conventional FEA.

The elastic stretchability is the applied strain when the maximum strain in the interconnect reaches the yield strain (0.3%, William et al., 1999) of the material. Fig. 6 shows the elastic stretchability versus the order n of fractal interconnects for $\eta = 8/\sqrt{11}$ and $m = 4$. The thickness/width aspect ratio in the cross section is $t/w = 0.03$, and the width to spacing ratio is $w/l^{(1)} = 0.4$. The results agree very well with conventional FEA for $n \leq 3$. For each increase of n by 1, the elastic stretchability

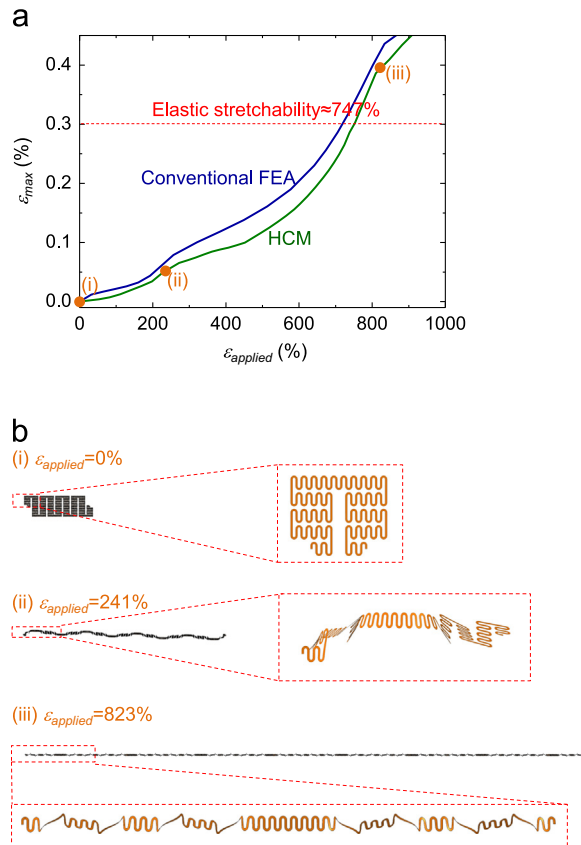


Fig. 9. (a) Maximum principal strain versus the applied strain for a 3rd order fractal interconnect with $(m, \eta) = (4, 8/\sqrt{11})$ and $w/l^{(1)} = 0.4$ and (b) the undeformed and deformed configurations when the 3rd and 2nd order structures are fully unraveled.

increases by > 3 times, suggesting that the high-order fractal design can substantially improve the elastic limit. For example, the elastic stretchability increases ~ 200 times, from $\sim 10.7\%$ for the 1st order, to $\sim 2140\%$ for the 4th order. The computational times required to finish the postbuckling analyses of the 3rd order fractal interconnect are also recorded, by using the same computer (with 8 CPUs) and applied strain ($\sim 850\%$). It turns out that the time cost (~ 146 min) of the HCM is much shorter than that (2340 min) of conventional FEA.

Figs. 7–10 show the maximum principal strain in the fractal interconnect and the evolution of deformation patterns for the fractal order from 1 to 4, respectively. For the 1st order fractal interconnect (Fig. 7), the maximum principal strain increases rapidly with the applied strain, and quickly reaches the yield strain 0.3% , at which the interconnect is still far from complete unraveling and therefore leads to the elastic stretchability of only 10.7% . The width of interconnect plays an important role on the strain accumulation (Fig. 7b); and a narrower interconnect could relieve the strain level, leading to an enhanced elastic-stretchability ($\sim 17.6\%$ for $w/l^{(1)} = 0.2$, compared to $\sim 2.3\%$ for $w/l^{(1)} = 0.8$). The effect of width on the elastic-stretchability of 1st order serpentine interconnect can be described by a simple scaling law (Zhang et al., 2013b). For the 2nd order fractal interconnect (Fig. 8a), the maximum principal strain initially increases slowly when the unraveling starts with the 2nd order structure, but then exhibits “strain hardening” near the end of unraveling (of the 2nd order structure) (Fig. 8b) for the applied strain in range $150\% < \epsilon_{\text{applied}} < 240\%$. The yield strain 0.3% is reached during the strain hardening, which gives 192% elastic stretchability. For the 3rd order of fractal interconnect (Fig. 9a), there are two ranges of strain hardening, $150\% < \epsilon_{\text{applied}} < 240\%$ and $500\% < \epsilon_{\text{applied}} < 820\%$, corresponding to the (end of) unraveling of the highest (3rd) order and the next order (2nd) structures, respectively (Fig. 9b). The yield strain 0.3% is reached during the latter strain hardening (corresponding to the unraveling of 2nd order structures), which gives 747% elastic stretchability. As compared to Fig. 9a, the 4th order fractal interconnect (Fig. 10a) exhibits an additional range of strain hardening ($1500\% < \epsilon_{\text{applied}} < 2300\%$), and its three ranges of strain hardening correspond to the (end of) unraveling of the 4th, 3rd and 2nd order structures, respectively (Fig. 10b). The elastic stretchability 2140% is reached during the last strain hardening event (corresponding to the unraveling of 2nd order structures). It is clear that the ordered unraveling of fractal interconnects significantly retards the rate of increase of maximum principal strain, and therefore enables large elastic

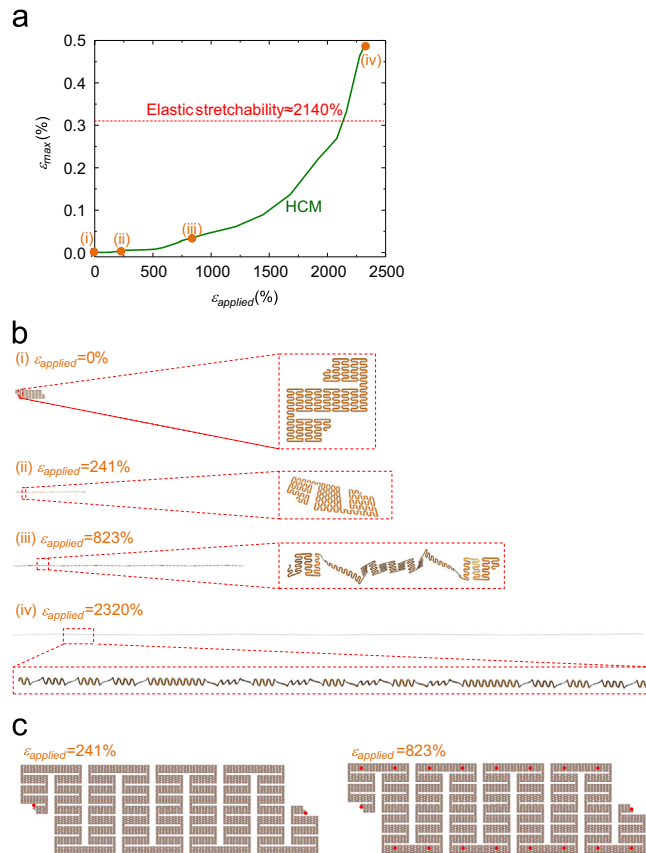


Fig. 10. (a) Maximum principal strain versus the applied strain for a 4th order fractal interconnect with $(m, \eta) = (4, 8/\sqrt{11})$ and $w/l^{(1)} = 0.4$, (b) the undeformed and deformed configurations when the 4th, 3rd and 2nd order structures are fully unraveled and (c) location of maximum principal strain at two different applied strains, as indicated by the red dots. (For interpretation of the references to color in this figure legend, the reader is referred to the web version of this article.)

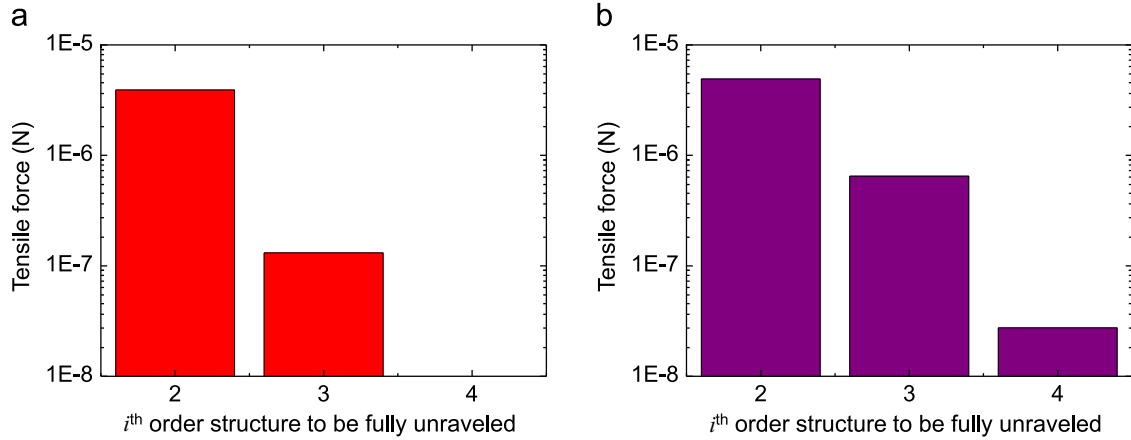


Fig. 11. Tensile force required to unravel fully the i th order structure in a 3rd order (a) and 4th order (b) fractal interconnect, with $(m, \eta) = (4, 8/\sqrt{11})$, $w = 20 \mu\text{m}$ and $l^{(1)} = 50 \mu\text{m}$.

stretchability. The location of maximum principal strain also shifts as the unraveling process evolves. Fig. 10c demonstrates the location of maximum principal strain at two typical applied strains, where multiple points are marked in the right frame, because of the structural periodicity after full unraveling of the 4th order structure. Such shift in the location of maximum strain can be mainly attributed to the remarkable change of geometric configuration during the stretching process.

It should be pointed out that this level of interconnect stretchability (2140%) translates to 110% elastic stretchability of the system for $\sim 90\%$ filling ratio of active devices based on Eq. (1), and 22% for 98% filling ratio, which are sufficient for biomedical applications.

The tensile force to unravel the fractal interconnects also increases with the stretching proceeds. Fig. 11 shows the tensile force required to unravel fully the various levels of the fractal structure for the 3rd and 4th order fractal interconnects studied in Figs. 9 and 10. As the fractal serpentine interconnect gets unraveled into lower-order structures, the tensile force increases tremendously, because of the increase in the structural stiffness. For a 4th order interconnect (in Fig. 11b), the force required to fully unravel the 2nd order structure is ~ 7.6 times and ~ 179.6 times larger than that required to unravel fully the 3rd and 4th order structures, respectively.

5. Generalized fractal interconnects

The fractal interconnects discussed above can be generalized such that at each order the interconnect may have its own height/spacing aspect ratios $\eta^{(i)}$ and number of unit cells $m^{(i)}$ ($i=1,2,\dots,n$). The generalized fractal interconnects may provide simultaneously large elastic stretchability and a relatively low electrical resistance, as demonstrated in Xu et al. (2013). For the n th order generalized fractal interconnect, the geometric relation (2) becomes

$$l^{(i)} = \left[\prod_{k=1}^{n-i} \frac{\eta^{(n-k+1)}}{2m^{(n-k)}} \right] l^{(n)}, \quad h^{(i)} = \eta^{(i)} \left[\prod_{k=1}^{n-i} \frac{\eta^{(n-k+1)}}{2m^{(n-k)}} \right] l^{(n)} \quad (i=1 \dots n-1) \quad (8)$$

The HCM introduced in Section 3 can be extended straightforwardly to study the postbuckling of a generalized fractal interconnect. Fig. 12 shows a generalized 2nd order fractal interconnect in the experiments (Xu et al., 2013) of stretchable battery. The interconnect, as shown at the top of Fig. 12 ($\varepsilon=0\%$), is composed of two polyimide (PI) layers (both $1.2 \mu\text{m}$ in thickness, $E_{PI}=2.5 \text{ GPa}$ and $\nu_{PI}=0.34$) that sandwich the conducting copper layer ($0.6 \mu\text{m}$ in thickness). The metal trace is connected by two rigid, circular islands, which hardly deform during the stretching of the entire structure.

Fig. 12 compares the optical images from experiments to the results obtained by the HCM on the deformed configurations of the fractal interconnect, for two different buckling modes, i.e., the symmetric and anti-symmetric modes. Good agreement between HCM and experiments are observed over the entire range of stretching (0–300%) for both modes. The maximum strain in the metal layer obtained by the HCM agrees well with that obtained by conventional FEA (Fig. 13), but the former is much faster and is applicable to higher fractal orders. The experiments (Fig. 12) and conventional FEA (Fig. 13) clearly validate the HCM.

6. Conclusions and discussions

A hierarchical computational model for postbuckling analysis of fractal interconnects based on the mechanism of ordered unraveling is developed in this paper. The approach substantially reduces the computational efforts and costs compared to

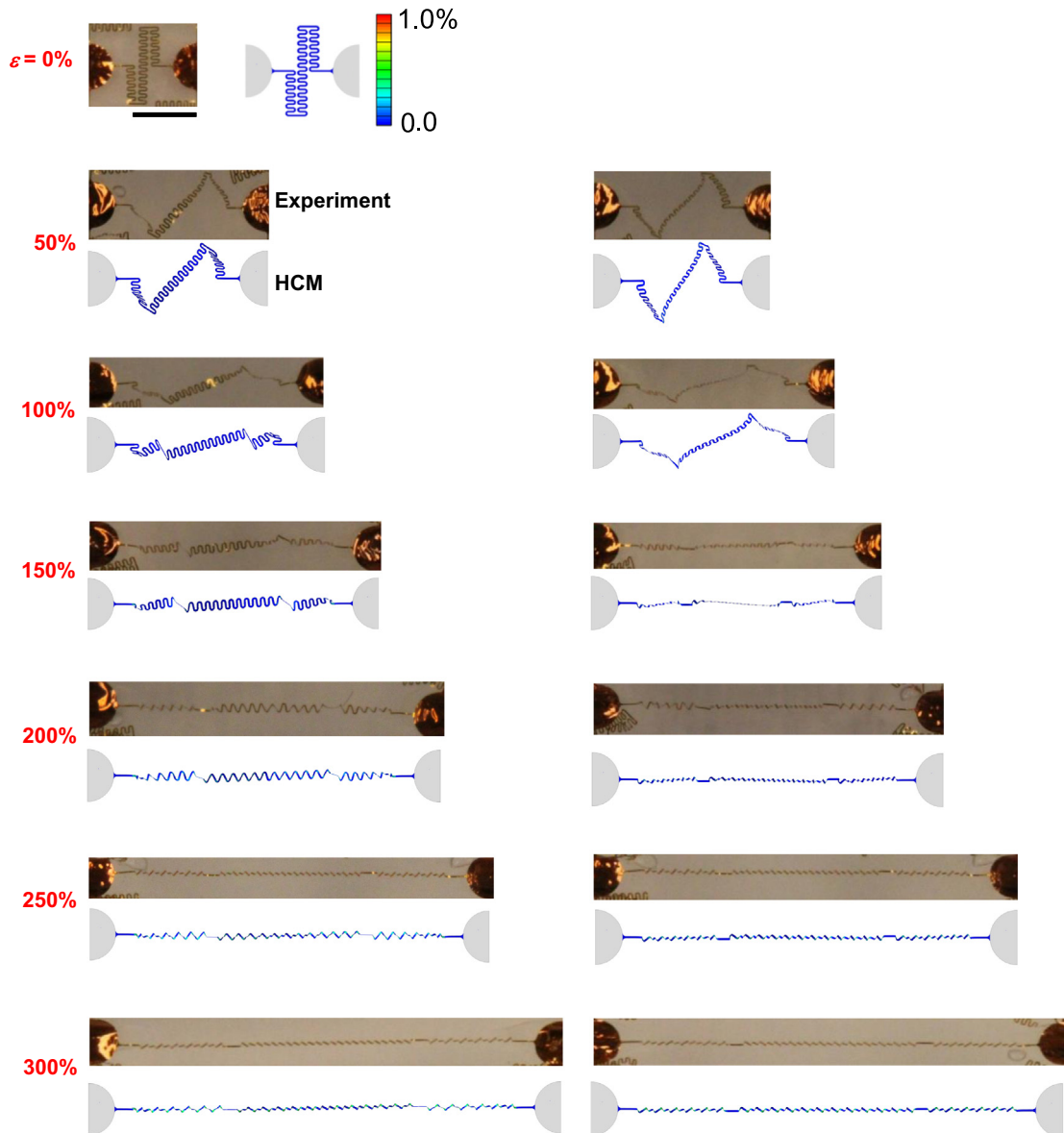


Fig. 12. Symmetric (left panel) and anti-symmetric (right panel) deformation modes from experiments (Xu et al., 2013) and numerical results by the HCM, for various levels of applied tensile strain ($0 \leq \epsilon \leq 300\%$). The scale bar is 2 mm.

conventional FEA, but with accurate predictions, as validated by both experiments and FEA. The designs provide large enhancements (by ~ 200 times) in the elastic stretchability, as the fractal order increases from 1 to 4. The HCM is also applicable to many other types of fractal layouts formed without intersection points, such as Peano and Hilbert curves (Sagan, 1994). It is useful for the development of stretchable electronics that simultaneously demand large areal coverage of active devices, such as stretchable photovoltaics (Yoon et al., 2008) and electronic eye-ball cameras (Ko et al., 2008). The concept of fractal interconnects could be further combined with other strategies for stretchability, such as prestraining of soft substrate (Lee et al., 2011b; Zhang et al., 2014), to further enhance the stretchability.

It should be pointed out that processes of ordered unraveling play critical roles in the enhanced elastic stretchability of high-order fractal interconnects, far beyond the simple increase of total length of interconnects with the fractal order. For example, the 1st and 2nd order fractal interconnects in Fig. 14 have the same total length and cross-section (width and thickness) and the same spacing between the device islands, yet the 2nd order interconnect outperforms the 1st order one in the elastic-stretchability by nearly a factor of 2 (528% versus 284%) (Xu et al., 2013).

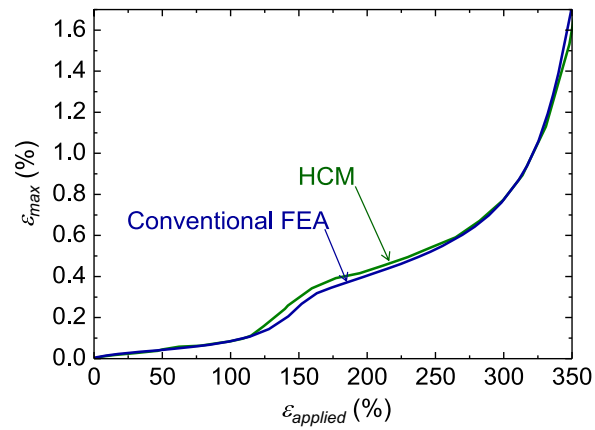


Fig. 13. The maximum principal strain in the metal layer versus the applied strain from conventional FEA and the HCM, for the fractal interconnects adopted in the experiment of Xu et al. (2013).

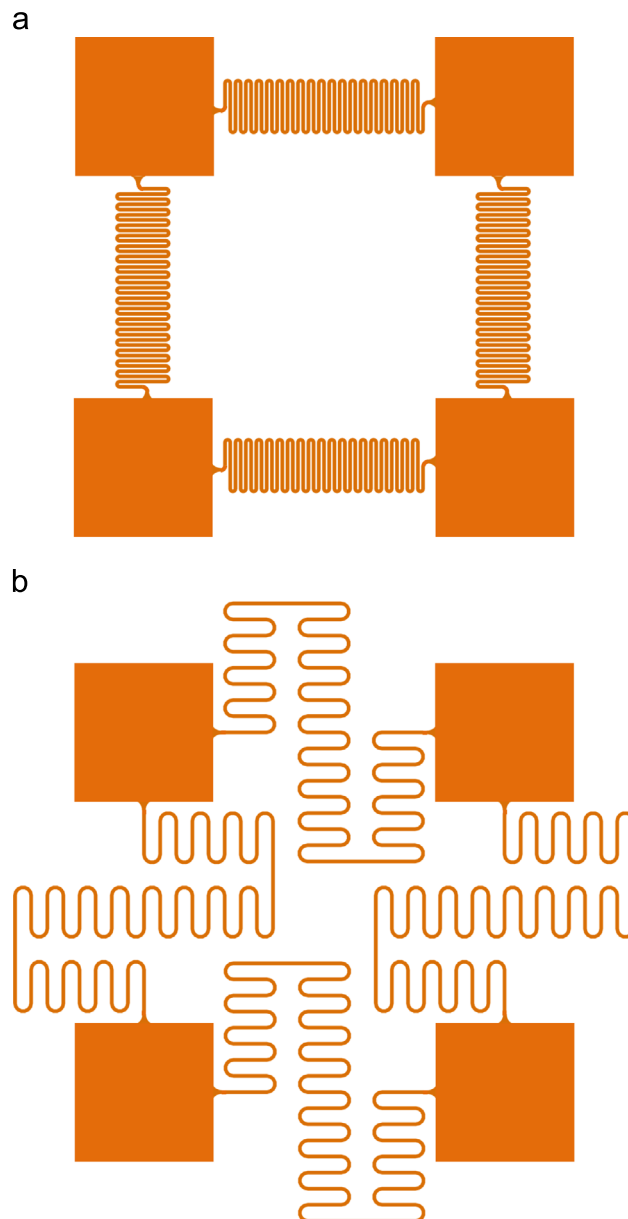


Fig. 14. The 1st (a) and 2nd (b) order fractal interconnects, with the same total length (16.77 mm) of interconnect, spacing (1.6 mm) between the device islands, height (0.4 mm) of the 1st order interconnect, width ($w=30\ \mu\text{m}$), and thickness ($t=3.0\ \mu\text{m}$).

Acknowledgments

Y.H. acknowledges the support from ISEN at Northwestern University. The support from NSFC is also acknowledged.

Appendix A. The effective flexibility of an n th order fractal interconnect

For the 1st order fractal interconnect clamped at the left end and subject to forces (N, Q_y, Q_z) and bending moments (M_x, M_y, M_z) at the right end, the strain energy of the entire interconnect can be obtained from summation of the bending energy in all straight and curved parts (Zhang et al., 2013a). The flexibility matrices $\mathbf{T}_{in-plane}^{(1)}$ and $\mathbf{T}_{out-of-plane}^{(1)}$ of the 1st order interconnect can be obtained from the 2nd order derivative of the strain energy function with respect to the components of force (or bending moment), as given in Eqs. (4a) and (4b).

The 2nd order fractal interconnect is composed of vertically aligned 1st order interconnects and horizontally aligned straight beams. Its strain energy is the sum of that in all 1st order interconnects and straight beams, whereas the strain energy of 1st order interconnect can be obtained using its flexibility matrices, $\mathbf{T}_{in-plane}^{(1)}$ and $\mathbf{T}_{out-of-plane}^{(1)}$. On the other hand, the strain energy of the 2nd order fractal interconnect can be given in terms of the $\mathbf{T}_{in-plane}^{(2)}$ and $\mathbf{T}_{out-of-plane}^{(2)}$. This energy equivalence leads to the analytical expression of $\mathbf{T}_{in-plane}^{(2)}$ and $\mathbf{T}_{out-of-plane}^{(2)}$ in Eqs. (5a) and (5b), where the component $T_{out-of-plane,11}^{(2)}$ is given by

$$T_{out-of-plane,11}^{(2)} = \frac{m^3}{3} [4p - (1 - \nu)\pi\eta] + \frac{m}{12}\eta [k(\eta^2 + 2) + (5 + \nu)\eta - 2(1 - \nu)] \\ + \frac{\eta^3}{384m} \{8\eta p + [(5 + 3\nu)\pi - 16](p - \pi\eta) + 8[8(1 + \nu) - \pi]\eta + 2(7 + 5\nu)\pi - 16(3 + 4\nu)\}. \quad (A.1)$$

An order- n interconnect is composed of vertically aligned order- $(n-1)$ interconnects, and horizontally aligned order- $(n-2)$ order interconnects. Based on the equivalence of strain energy of the order- n interconnect and that from summation of strain energy in all order- $(n-1)$ and order- $(n-2)$ interconnects, $\mathbf{T}_{in-plane}^{(n)}$ and $\mathbf{T}_{out-of-plane}^{(n)}$ are obtained in the following recursive formula via the flexibility matrices for the $(n-1)$ th and $(n-2)$ th order:

$$\mathbf{T}_{in-plane}^{(n)} = \frac{\eta}{2m} \begin{pmatrix} \frac{\eta}{2m} & 0 & 0 \\ 0 & \frac{\eta}{2m} & 0 \\ 0 & 0 & 1 \end{pmatrix} \sum_{k=1}^m \left\{ \bar{\mathbf{D}}_I [\mathbf{T}_{in-plane}^{(n-1)} \mathbf{K}_1(m) + \mathbf{K}_1^T(m) \mathbf{T}_{in-plane}^{(n-1)}] \bar{\mathbf{D}}_I^T \right. \\ \left. + \bar{\mathbf{D}}_{II} \mathbf{T}_{in-plane}^{(n-1)} \bar{\mathbf{D}}_{II}^T \right. \\ \left. + \bar{\mathbf{D}}_{III} [\mathbf{T}_{in-plane}^{(n-1)} \mathbf{K}_1(m) + \mathbf{K}_1^T(m) \mathbf{T}_{in-plane}^{(n-1)}] \bar{\mathbf{D}}_{III}^T \right\} \begin{pmatrix} \frac{\eta}{2m} & 0 & 0 \\ 0 & \frac{\eta}{2m} & 0 \\ 0 & 0 & 1 \end{pmatrix} \\ + \frac{\eta^2}{4m^2} \sum_{k=1}^m [\bar{\mathbf{D}}_{IV}^* \mathbf{T}_{in-plane}^{(n-2)} \bar{\mathbf{D}}_{IV}^{*T} + \bar{\mathbf{D}}_V^* \mathbf{T}_{in-plane}^{(n-2)} \bar{\mathbf{D}}_V^{*T}] \quad \text{for } n \geq 3 \quad (A.2a)$$

$$\mathbf{T}_{out-of-plane}^{(n)} = \frac{\eta}{2m} \begin{pmatrix} \frac{\eta}{2m} & 0 & 0 \\ 0 & 1 & 0 \\ 0 & 0 & 1 \end{pmatrix} \sum_{k=1}^m \left\{ \bar{\mathbf{R}}_I [\mathbf{T}_{out-of-plane}^{(n-1)} \mathbf{K}_2(m) + \mathbf{K}_2^T(m) \mathbf{T}_{out-of-plane}^{(n-1)}] \bar{\mathbf{R}}_I^T \right. \\ \left. + \bar{\mathbf{R}}_{II} \mathbf{T}_{out-of-plane}^{(n-1)} \bar{\mathbf{R}}_{II}^T \right. \\ \left. + \bar{\mathbf{R}}_{III} [\mathbf{T}_{out-of-plane}^{(n-1)} \mathbf{K}_2(m) + \mathbf{K}_2^T(m) \mathbf{T}_{out-of-plane}^{(n-1)}] \bar{\mathbf{R}}_{III}^T \right\} \begin{pmatrix} \frac{\eta}{2m} & 0 & 0 \\ 0 & 1 & 0 \\ 0 & 0 & 1 \end{pmatrix} \\ + \frac{\eta^2}{4m^2} \sum_{k=1}^m [\bar{\mathbf{R}}_{IV}^* \mathbf{T}_{out-of-plane}^{(n-2)} \bar{\mathbf{R}}_{IV}^{*T} + \bar{\mathbf{R}}_V^* \mathbf{T}_{out-of-plane}^{(n-2)} \bar{\mathbf{R}}_V^{*T}] \quad \text{for } n \geq 3 \quad (A.2b)$$

where

$$\bar{\mathbf{D}}_I = \begin{bmatrix} 0 & 1 & -m \\ 1 & 0 & -4(m-k+1)m\eta^{-1} \\ 0 & 0 & -1 \end{bmatrix}, \quad \bar{\mathbf{D}}_{II} = \begin{bmatrix} 0 & 1 & -m \\ -1 & 0 & (4m-4k+2)m\eta^{-1} \\ 0 & 0 & 1 \end{bmatrix}, \\ \bar{\mathbf{D}}_{III} = \begin{bmatrix} 0 & 1 & 0 \\ 1 & 0 & -4(m-k)m\eta^{-1} \\ 0 & 0 & -1 \end{bmatrix}, \quad \bar{\mathbf{D}}_{IV}^* = \begin{bmatrix} \eta^2/(4m^2) & 0 & \eta/2 \\ 0 & \eta^2/(4m^2) & 2m-2k+1 \\ 0 & 0 & 1 \end{bmatrix},$$

$$\bar{\mathbf{D}}_V^* = \begin{bmatrix} \eta^2/(4m^2) & 0 & \eta/2 \\ 0 & -\eta^2/(4m^2) & -2m+2k \\ 0 & 0 & -1 \end{bmatrix}, \quad \mathbf{K}_1(m) = \frac{1}{4} \begin{pmatrix} 1 & 0 & 0 \\ 0 & 1 & 0 \\ 0 & -m & 1 \end{pmatrix},$$

$$\bar{\mathbf{R}}_I = \begin{bmatrix} 1 & m & -4(m-k+1)m\eta^{-1} \\ 0 & 0 & 1 \\ 0 & -1 & 0 \end{bmatrix}, \quad \bar{\mathbf{R}}_{II} = \begin{bmatrix} 1 & m & (4m-4k+2)m\eta^{-1} \\ 0 & 0 & -1 \\ 0 & 1 & 0 \end{bmatrix},$$

$$\bar{\mathbf{R}}_{III} = \begin{bmatrix} 1 & 0 & -4(m-k)m\eta^{-1} \\ 0 & 0 & 1 \\ 0 & -1 & 0 \end{bmatrix}, \quad \bar{\mathbf{R}}_{IV}^* = \begin{bmatrix} \eta^2/(4m^2) & -(2m-2k+1) & -\eta^3/(8m^2) \\ 0 & \eta^2/(4m^2) & 0 \\ 0 & 0 & \eta^2/(4m^2) \end{bmatrix},$$

$$\bar{\mathbf{R}}_V^* = \begin{bmatrix} \eta^2/(4m^2) & -(2m-2k) & -\eta^3/(8m^2) \\ 0 & \eta^2/(4m^2) & 0 \\ 0 & 0 & -\eta^2/(4m^2) \end{bmatrix} \text{ and } \mathbf{K}_2(m) = \frac{1}{4} \begin{pmatrix} 1 & 0 & 0 \\ m & 1 & 0 \\ 0 & 0 & 1 \end{pmatrix}.$$

References

- Cotton, D.P.J., Graz, I.M., Lacour, S.P., 2009. A multifunctional capacitive sensor for stretchable electronic skins. *IEEE Sens. J.* 9, 2008–2009.
- Duan, Y.Q., Huang, Y.A., Yin, Z.P., Bu, N.B., Dong, W.T., 2014. Non-wrinkled, highly stretchable piezoelectric devices by electrohydrodynamic direct-writing. *Nanoscale* 6, 3289–3295. <http://dx.doi.org/10.1039/C3NR06007A>.
- Gao, H.J., Wang, X., Yao, H.M., Gorb, S., Arzt, E., 2005. Mechanics of hierarchical adhesion structures of geckos. *Mech. Mater.* 37, 275–285.
- Gonzalez, M., Axisa, F., Bulcke, M.V., Brosteaux, D., Vandeveld, B., Vanfleteren, J., 2008. Design of metal interconnects for stretchable electronic circuits. *Microelectron. Reliabil.* 48, 825–832.
- Graudejus, O., Morrison, B., Goletiani, C., Yu, Z., Wagner, S., 2012. Encapsulating elastically stretchable neural interfaces: yield, resolution, and recording/stimulation of neural activity. *Adv. Funct. Mater.* 22, 640–651.
- Hsu, Y.Y., Gonzalez, M., Bossuyt, F., Axisa, F., Vanfleteren, J., De Wolf, I., 2009. In situ observations on deformation behavior and stretching-induced failure of fine pitch stretchable interconnect. *J. Mater. Res.* 24, 3573–3582.
- Huang, Y.A., Wang, X.M., Duan, Y.Q., Bu, N.B., Yin, Z.P., 2012. Controllable self-organization of colloid microarrays based on finite length effects of electrospun ribbons. *Soft Matter* 8, 8302–8311.
- Jiang, H.Q., Khang, D.Y., Fei, H.Y., Kim, H., Huang, Y.G., Xiao, J.L., Rogers, J.A., 2008. Finite width effect of thin-films buckling on compliant substrate: experimental and theoretical studies. *J. Mech. Phys. Solids* 56, 2585–2598.
- Jiang, H.Q., Khang, D.Y., Song, J.Z., Sun, Y.G., Huang, Y.G., Rogers, J.A., 2007. Finite deformation mechanics in buckled thin films on compliant supports. *Proc. Natl. Acad. Sci. USA* 104, 15607–15612.
- Jones, J., Lacour, S.P., Wagner, S., Suo, Z.G., 2004. Stretchable wavy metal interconnects. *J. Vac. Sci. Technol. A* 22, 1723–1725.
- Kaltenbrunner, M., Sekitani, T., Reeder, J., Yokota, T., Kuribara, K., Tokuhara, T., Drack, M., Schwodiauer, R., Graz, I., Bauer-Gogonea, S., Bauer, S., Someya, T., 2013. An ultra-lightweight design for imperceptible plastic electronics. *Nature* 499, 458–463.
- Khang, D.Y., Jiang, H.Q., Huang, Y., Rogers, J.A., 2006. A stretchable form of single-crystal silicon for high-performance electronics on rubber substrates. *Science* 311, 208–212.
- Kim, D.H., Ghaffari, R., Lu, N.S., Wang, S.D., Lee, S.P., Keum, H., D'Angelo, R., Klinker, L., Su, Y.W., Lu, C.F., Kim, Y.S., Ameen, A., Li, Y.H., Zhang, Y.H., de Graff, B., Hsu, Y.Y., Liu, Z.J., Ruskin, J., Xu, L.Z., Lu, C., Omenetto, F.G., Huang, Y.G., Mansour, M., Slepian, M.J., Rogers, J.A., 2012a. Electronic sensor and actuator webs for large-area complex geometry cardiac mapping and therapy. *Proc. Natl. Acad. Sci. USA* 109, 19910–19915.
- Kim, D.H., Liu, Z.J., Kim, Y.S., Wu, J., Song, J.Z., Kim, H.S., Huang, Y.G., Hwang, K.C., Zhang, Y.W., Rogers, J.A., 2009. Optimized structural designs for stretchable silicon integrated circuits. *Small* 5, 2841–2847.
- Kim, D.H., Lu, N.S., Ghaffari, R., Kim, Y.S., Lee, S.P., Xu, L.Z., Wu, J.A., Kim, R.H., Song, J.Z., Liu, Z.J., Viventi, J., de Graff, B., Elolampi, B., Mansour, M., Slepian, M.J., Hwang, S., Moss, J.D., Won, S.M., Huang, Y.G., Litt, B., Rogers, J.A., 2011a. Materials for multifunctional balloon catheters with capabilities in cardiac electrophysiological mapping and ablation therapy. *Nat. Mater.* 10, 316–323.
- Kim, D.H., Lu, N.S., Ma, R., Kim, Y.S., Kim, R.H., Wang, S.D., Wu, J., Won, S.M., Tao, H., Islam, A., Yu, K.J., Kim, T.I., Chowdhury, R., Ying, M., Xu, L.Z., Li, M., Chung, H.J., Keum, H., McCormick, M., Liu, P., Zhang, Y.W., Omenetto, F.G., Huang, Y.G., Coleman, T., Rogers, J.A., 2011b. Epidermal electronics. *Science* 333, 838–843.
- Kim, D.H., Song, J.Z., Choi, W.M., Kim, H.S., Kim, R.H., Liu, Z.J., Huang, Y.Y., Hwang, K.C., Zhang, Y.W., Rogers, J.A., 2008. Materials and noncoplanar mesh designs for integrated circuits with linear elastic responses to extreme mechanical deformations. *Proc. Natl. Acad. Sci. USA* 105, 18675–18680.
- Kim, D.H., Wang, S.D., Keum, H., Ghaffari, R., Kim, Y.S., Tao, H., Panilaitis, B., Li, M., Kang, Z., Omenetto, F., Huang, Y.G., Rogers, J.A., 2012b. Thin, flexible sensors and actuators as 'instrumented' surgical sutures for targeted wound monitoring and therapy. *Small* 8, 3263–3268.
- Kim, R.H., Kim, D.H., Xiao, J.L., Kim, B.H., Park, S.I., Panilaitis, B., Ghaffari, R., Yao, J.M., Li, M., Liu, Z.J., Malyarchuk, V., Kim, D.G., Le, A.P., Nuzzo, R.G., Kaplan, D.L., Omenetto, F.G., Huang, Y.G., Kang, Z., Rogers, J.A., 2010. Waterproof AllnGaP optoelectronics on stretchable substrates with applications in biomedicine and robotics. *Nat. Mater.* 9, 929–937.
- Kim, R.H., Tao, H., Kim, T.I., Zhang, Y.H., Kim, S., Panilaitis, B., Yang, M.M., Kim, D.H., Jung, Y.H., Kim, B.H., Li, Y.H., Huang, Y.G., Omenetto, F.G., Rogers, J.A., 2012c. Materials and designs for wirelessly powered implantable light-emitting systems. *Small* 8, 2812–2818.
- Ko, H.C., Stoykovich, M.P., Song, J.Z., Malyarchuk, V., Choi, W.M., Yu, C.J., Geddes, J.B., Xiao, J.L., Wang, S.D., Huang, Y.G., Rogers, J.A., 2008. A hemispherical electronic eye camera based on compressible silicon optoelectronics. *Nature* 454, 748–753.
- Lacour, S.P., Jones, J., Wagner, S., Li, T., Suo, Z.G., 2005. Stretchable interconnects for elastic electronic surfaces. *Proc. IEEE* 93, 1459–1467.
- Lacour, S.P., Wagner, S., Narayan, R.J., Li, T., Suo, Z.G., 2006. Stiff subcircuit islands of diamondlike carbon for stretchable electronics. *J. Appl. Phys.* 100, 014913.
- Lee, C.H., Kim, Y.J., Hong, Y.J., Jeon, S.R., Bae, S., Hong, B.H., Yi, G.C., 2011a. Flexible inorganic nanostructure light-emitting diodes fabricated on graphene films. *Adv. Mater.* 23, 4614–4619.
- Lee, J., Wu, J.A., Shi, M.X., Yoon, J., Park, S.I., Li, M., Liu, Z.J., Huang, Y.G., Rogers, J.A., 2011b. Stretchable GaAs photovoltaics with designs that enable high areal coverage. *Adv. Mater.* 23, 986–991.
- Li, T., Suo, Z.G., Lacour, S.P., Wagner, S., 2005. Compliant thin film patterns of stiff materials as platforms for stretchable electronics. *J. Mater. Res.* 20, 3274–3277.
- Li, Y., Ortiz, C., Boyce, M.C., 2012. Bioinspired, mechanical, deterministic fractal model for hierarchical suture joints. *Phys. Rev. E*, 85.
- Li, Y., Ortiz, C., Boyce, M.C., 2013. A generalized mechanical model for suture interfaces of arbitrary geometry. *J. Mech. Phys. Solids* 61, 1144–1167.
- Lipomi, D.J., Tee, B.C.K., Vosgueritchian, M., Bao, Z.N., 2011. Stretchable organic solar cells. *Adv. Mater.* 23, 1771–1775.
- Lu, N.S., Lu, C., Yang, S.X., Rogers, J., 2012. Highly sensitive skin-mountable strain gauges based entirely on elastomers. *Adv. Funct. Mater.* 22, 4044–4050.

- Mannsfield, S.C. B., Tee, B.C. K., Stoltenberg, R.M., Chen, C., Barman, S., Muir, B.V. O., Sokolov, A.N., Reese, C., Bao, Z.N., 2010. Highly sensitive flexible pressure sensors with microstructured rubber dielectric layers. *Nat. Mater.* 9, 859–864.
- Nelson, E.C., Dias, N.L., Bassett, K.P., Dunham, S.N., Verma, V., Miyake, M., Wiltzius, P., Rogers, J.A., Coleman, J.J., Li, X.L., Braun, P.V., 2011. Epitaxial growth of three-dimensionally architected optoelectronic devices. *Nat. Mater.* 10, 676–681.
- Rogers, J.A., Someya, T., Huang, Y.G., 2010. Materials and mechanics for stretchable electronics. *Science* 327, 1603–1607.
- Sagan, H., 1994. *Space-filling Curves*. Springer-Verlag, New York.
- Schwartz, G., Tee, B.C. K., Mei, J.G., Appleton, A.L., Kim, D.H., Wang, H.L., Bao, Z.N., 2013. Flexible polymer transistors with high pressure sensitivity for application in electronic skin and health monitoring. *Nat. Commun.* 4, 1859.
- Sekitani, T., Nakajima, H., Maeda, H., Fukushima, T., Aida, T., Hata, K., Someya, T., 2009. Stretchable active-matrix organic light-emitting diode display using printable elastic conductors. *Nat. Mater.* 8, 494–499.
- Someya, T., Sekitani, T., Iba, S., Kato, Y., Kawaguchi, H., Sakurai, T., 2004. A large-area, flexible pressure sensor matrix with organic field-effect transistors for artificial skin applications. *Proc. Natl. Acad. Sci. USA* 101, 9966–9970.
- Song, J., Huang, Y., Xiao, J., Wang, S., Hwang, K.C., Ko, H.C., Kim, D.H., Stoykovich, M.P., Rogers, J.A., 2009. Mechanics of noncoplanar mesh design for stretchable electronic circuits. *J. Appl. Phys.* 105, 123516.
- Song, Y.M., Xie, Y.Z., Malyarchuk, V., Xiao, J.L., Jung, I., Choi, K.J., Liu, Z.J., Park, H., Lu, C.F., Kim, R.H., Li, R., Crozier, K.B., Huang, Y.G., Rogers, J.A., 2013. Digital cameras with designs inspired by the arthropod eye. *Nature* 497, 95–99.
- Viventi, J., Kim, D.H., Moss, J.D., Kim, Y.S., Blanco, J.A., Annetta, N., Hicks, A., Xiao, J.L., Huang, Y.G., Callans, D.J., Rogers, J.A., Litt, B., 2010. A conformal, bio-interfaced class of silicon electronics for mapping cardiac electrophysiology. *Sci. Transl. Med.* 2, 24ra22.
- Wagner, S., Lacour, S.P., Jones, J., Hsu, P.H. I., Sturm, J.C., Li, T., Suo, Z.G., 2004. Electronic skin: architecture and components. *Physica E-Low-Dimens. Syst. Nanostruct.* 25, 326–334.
- Webb, R.C., Bonifas, A.P., Behnaz, A., Zhang, Y.H., Yu, K.J., Cheng, H.Y., Shi, M.X., Bian, Z.G., Liu, Z.J., Kim, Y.S., Yeo, W.H., Park, J.S., Song, J.Z., Li, Y.H., Huang, Y.G., Gorbach, J.A., Rogers, J.A., 2013. Ultrathin conformal devices for precise and continuous thermal characterization of human skin. *Nat. Mater.* 12, 938–944.
- William, F.R., Leroy, D.S., Don, H.M., 1999. *Mechanics of Materials*. John Wiley & Sons, New York.
- Xu, S., Zhang, Y.H., Cho, J., Lee, J., Huang, X., Jia, L., Fan, J.A., Su, Y.W., Su, J., Zhang, H.G., Cheng, H.Y., Lu, B.W., Yu, C.J., Chuang, C., Kim, T.I., Song, T., Shigeta, K., Kang, S., Dagdeviren, C., Petrov, I., Braun, P.V., Huang, Y., Paik, U., Rogers, J.A., 2013. Stretchable batteries with self-similar serpentine interconnects and integrated wireless recharging systems. *Nat. Commun.* 4, 1543.
- Yang, S.X., Lu, N.S., 2013. Gauge factor and stretchability of silicon-on-polymer strain gauges. *Sensors* 13, 8577–8594.
- Yao, H., Gao, H., 2006. Mechanics of robust and releasable adhesion in biology: bottom-up designed hierarchical structures of gecko. *J. Mech. Phys. Solids* 54, 1120–1146.
- Yao, H., Gao, H., 2007. Multi-scale cohesive laws in hierarchical materials. *Int. J. Solids Struct.* 44, 8177–8193.
- Ying, M., Bonifas, A.P., Lu, N.S., Su, Y.W., Li, R., Cheng, H.Y., Ameen, A., Huang, Y.G., Rogers, J.A., 2012. Silicon nanomembranes for fingertip electronics. *Nanotechnology* 23, 344004.
- Yoon, J., Baca, A.J., Park, S.I., Elvikis, P., Geddes, J.B., Li, L.F., Kim, R.H., Xiao, J.L., Wang, S.D., Kim, T.H., Motala, M.J., Ahn, B.Y., Duoss, E.B., Lewis, J.A., Nuzzo, R.G., Ferreira, P.M., Huang, Y.G., Rockett, A., Rogers, J.A., 2008. Ultrathin silicon solar microcells for semitransparent, mechanically flexible and microconcentrator module designs. *Nat. Mater.* 7, 907–915.
- Yu, Z., Graudejus, O., Tsay, C., Lacour, S.P., Wagner, S., Morrison, B., 2009. Monitoring hippocampus electrical activity in vitro on an elastically deformable microelectrode array. *J. Neurotrauma* 26, 1135–1145.
- Zhang, Y.H., Fu, H.R., Su, Y.W., Xu, S., Cheng, H.Y., Fan, J.A., Hwang, K.C., Rogers, J.A., Huang, Y., 2013a. Mechanics of ultra-stretchable self-similar serpentine interconnects. *Acta Mater.* 61, 7816–7827.
- Zhang, Y.H., Xu, S., Fu, H.R., Lee, J., Su, J., Hwang, K.C., Rogers, J.A., Huang, Y., 2013b. Buckling in serpentine microstructures and applications in elastomer-supported ultra-stretchable electronics with high areal coverage. *Soft Matter* 9, 8062–8070.
- Zhang, Y.H., Wang, S.D., Li, X.T., Fan, J.A., Xu, S., Song, Y.M., Choi, K.J., Yeo, W.H., Lee, W., Nazaar, S.N., Lu, B.W., Yin, L., Hwang, K.C., Rogers, J.A., Huang, Y., 2014. Experimental and theoretical studies of serpentine microstructures bonded to prestrained elastomers for stretchable electronics. *Adv. Funct. Mater.* 24, 2028–2037.
- Zhang, Z., Zhang, T., Zhang, Y.W., Kim, K.-S., Gao, H., 2012. Strain-controlled switching of hierarchically wrinkled surfaces between superhydrophobicity and superhydrophilicity. *Langmuir* 28, 2753–2760.
- Zhang, Z., Zhang, Y.-W., Gao, H., 2011. On optimal hierarchy of load-bearing biological materials. *Proc. R. Soc. B-Biol. Sci.* 278, 519–525.